

Experimental summary

Pierre Van Mechelen

Universiteit Antwerpen, Belgium

DOI: <http://dx.doi.org/10.3204/DESY-PROC-2009-01/88>

Abstract

A selection of experimental results contributed to the XXXVIIIth International Symposium on Multiparticle Dynamics is presented. Following the working group structure of the symposium, emphasis is put on dilute systems, the interpolation region, dense systems, strategies and analysis methods and new physics.

1 Dilute systems

In many cases, the proton is considered to be a dilute system of quarks and gluons, bound together by the strong interaction. This is because, to a good approximation, the densities of quarks and gluons inside the proton can be well described by linear QCD evolution equations, yielding the dependence of the parton densities on the resolution scale Q^2 and the fraction x of the proton momentum carried by the parton. This linear approximation should be valid if the probability for parton recombination or multiple scattering is small, as is the case in a dilute system.

The description of interactions with dilute protons in perturbative QCD can be factorised in two parts. First, the matrix element is an exact calculation of the partonic cross section up to a fixed order in perturbation theory. Nowadays, calculations up to $O(\alpha_S^3)$ are possible. Second, this partonic cross section is convoluted with the density of partons with certain kinematics, given by x and Q^2 . The error made by neglecting higher orders in the calculation of the matrix element can be covered by so-called parton showers or evolution equations for the parton densities, which sum a subset of (leading) diagrams at each order. Which diagrams are leading depends on the kinematics of the process and different approaches therefore exist. The DGLAP approach [1] will resum terms proportional to $[\alpha_S \ln Q^2/Q_0^2]^n$, with Q_0^2 a fixed, low starting scale, and is therefore relevant to processes at large Q^2 . The BFKL approach [2] on the other hand resums terms proportional to $[\alpha_S \ln 1/x]^n$ and should be used for process at low x . Other approaches, combining elements of the former two, like the CCFM approach [3], also exist.

This section reviews results, presented at ISMD08, on parton densities and linear parton dynamics. The extraction of parton densities is dominated by data on inclusive deep inelastic ep scattering. As will be shown, a standard DGLAP analysis of the data works well. Signals of different parton dynamics are best obtained by looking at specific final states by applying cuts to enhance the phase space for non-DGLAP dynamics.

1.1 Structure functions and parton distributions

The HERA experiments have studied the structure of the proton extensively through the measurement of the deep inelastic electron¹-proton scattering cross section. As is well known, the

¹“Electron” is used here as a generic name for both electrons and positrons.

differential cross section can be expressed as a function of the structure functions F_2 , F_L and F_3 :

$$\frac{d^2\sigma(e^\pm p)}{dx dQ^2} = \frac{2\pi\alpha^2}{xQ^4} Y_+ \left[F_2(x, Q^2) - \frac{y^2}{Y_+} F_L(x, Q^2) \pm xF_3(x, Q^2) \right], \quad (1)$$

where the kinematic variables are defined as $Q^2 = -q^2 = -(k - k')^2$, $x = \frac{Q^2}{2P \cdot q}$ and $y = \frac{P \cdot q}{P \cdot k}$, with P , k , and k' the four-momenta of the incoming proton, incoming electron and scattered electron, respectively. For brevity, one further defines $Y_+ = \frac{(1+(1-y)^2)}{2}$.

The careful combination of HERA-I data obtained by the H1 and ZEUS collaborations has greatly improved the precision of the measurement of F_2 [4]. Some representative results are shown in Fig. 1 (left). Systematic uncertainties are now smaller than the statistical errors across the x, Q^2 plane. This combined data set has been subjected to a NLO DGLAP fit and yields parton density functions (PDFs) with impressive precision (shown in Fig. 1 (right)).

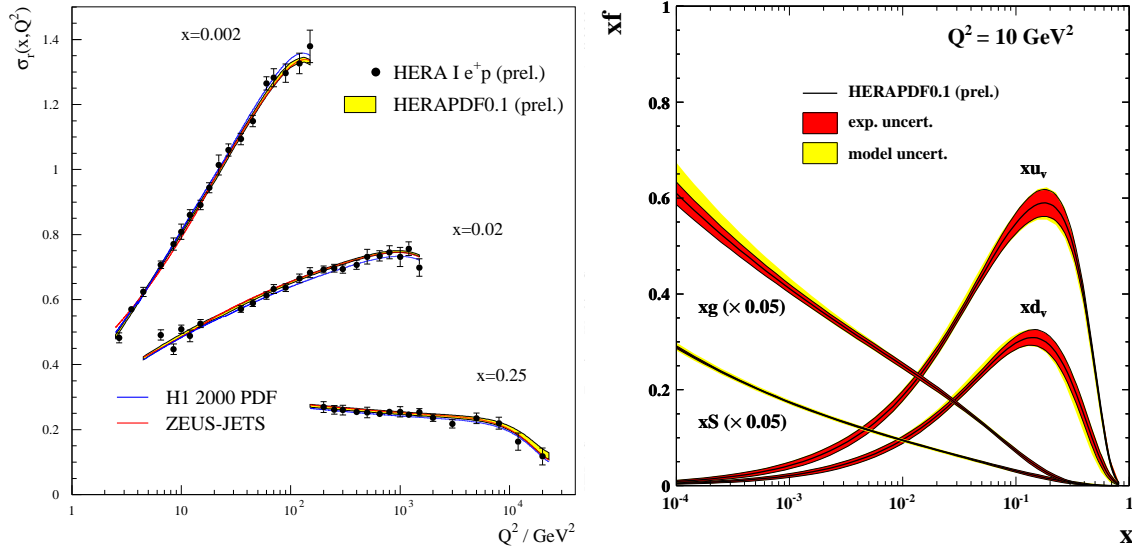


Fig. 1: (left) The neutral current reduced cross section $\sigma_r = \frac{xQ^4}{2\pi\alpha^2 Y_+} \frac{d^2\sigma(e^\pm p)}{dx dQ^2}$ vs. Q^2 for three x -bins. The prediction of the HERAPDF0.1 fit are superimposed, together with predictions of the H1PDF2000 and ZEUS-JETS PDFs as obtained in NLO QCD fits to the inclusive H1 data and to the inclusive and jet ZEUS data, respectively. (right) HERAPDF 0.1 PDFs from the analysis of the combined data set.

Figure 2 (left) shows a measurement of xF_3 [5], which is the parity-violating term in Eq. (1) arising from Z exchange. At HERA, this term is dominated by γ/Z interference rather than pure Z exchange. It can be experimentally extracted from the difference between the DIS cross section with electrons and positrons. F_3 should be approximately proportional to the valence quark density of the proton and thus peaks at relatively large fractional momenta x .

It should be noted that the HERA-I running period only corresponds to about one third of the total integrated luminosity. The final analysis of the proton structure by H1 and ZEUS will be based on some 1 fb^{-1} of data for both experiments together.

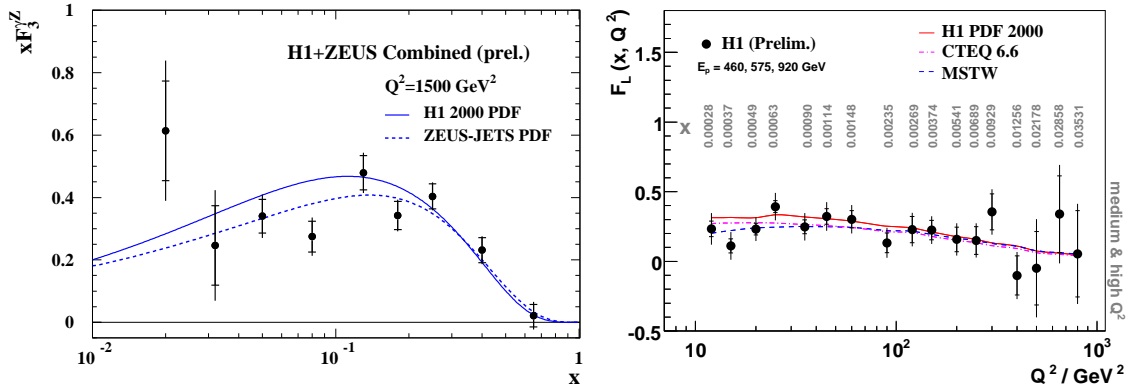


Fig. 2: (left) Combined H1/ZEUS measurement of the structure function $xF_3^{\gamma/Z}$. The curves describe the Standard Model predictions based on the H1PDF2000 and ZEUS-JETS PDFs. (right) The longitudinal structure function F_L averaged in x at given values of Q^2 . The resulting x values of the averaged F_L measurements are given in the figure for each point in Q^2 . The solid line represents a QCD prediction based on the H1PDF2000 fit. The dashed line represent the MSTW and the dashed-dotted line the CTEQ 6.6 predictions.

In order to extract the longitudinal structure function F_L , one needs to measure the DIS cross section at fixed x and Q^2 , but different y . Because of the relation $Q^2 = sxy$, this is only possible with different centre-of-mass energies \sqrt{s} . At the end of the HERA-II running period, a special run was performed with a lower proton beam energy, with the aim to measure F_L directly. As F_L is proportional to the gluon density at higher orders, one expects a direct sensitivity to gluon dynamics. Some of the obtained results are shown in Fig. 2 (right) [6]. The results are consistent with expectations from global parton distribution fits at higher order perturbation theory.

Although the HERA measurements are very precise, TEVATRON data can still help to further constrain QCD fits of the PDFs. E.g., the production of jets in $p\bar{p}$ collisions occurs preferentially through the $gg \rightarrow jets$ or $qg \rightarrow jets$ processes, and the measurement of the inclusive jet cross section at moderate E_T is therefore mostly sensitive to the gluon density at large fractional momenta. In contrast, at HERA the gluon density is inferred from scaling violations of F_2 and this yields comparatively large uncertainties at large x .

D0 has measured the jet cross section in Run-II data at large E_T and in different intervals of rapidity, as shown in Fig. 3 (left) [7]. Whereas earlier jet data showed a preference for a large gluon density at high x compared to global fits without TEVATRON jet data, the new data now prefer smaller high- x distribution. The variance in the gluon distribution at high x however still remains large [8].

The production of weak bosons in $p\bar{p}$ collisions occurs through the fusion of quark-anti-quark pairs. Contrary to DIS where the quark charge squared enters the expression of the cross section, the cross section for weak boson production does not depend on the quark charge and treats the u - and d -quark equally. Therefore, the measurement of W and Z production at the TEVATRON will have the greatest impact on the d -quark density. Fig. 3 (right) shows the rapidity distribution of Z/γ^* bosons as measured by CDF [9]. In spite of better constraints using Run-II

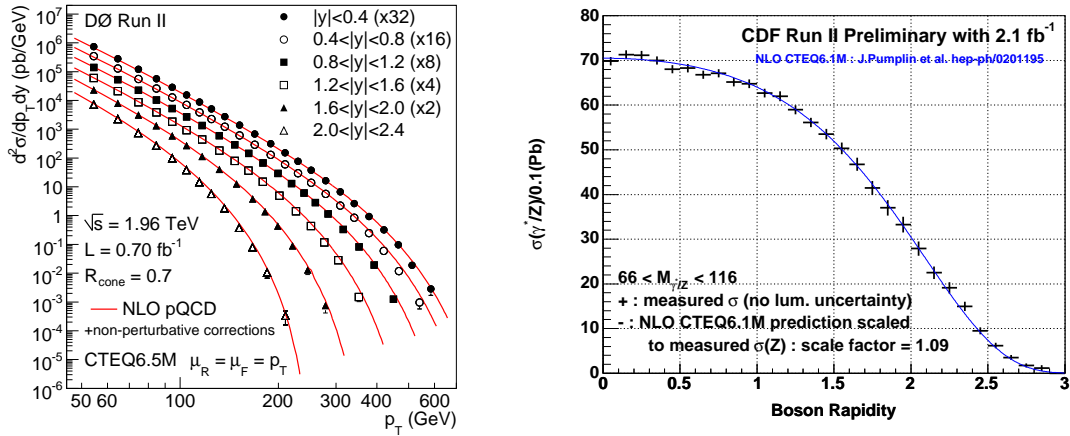


Fig. 3: (left) The inclusive jet cross section as a function of jet p_T in six $|y|$ bins. (right) Differential cross section $d\sigma/dy$ for $p\bar{p} \rightarrow Z^0/\gamma^* \rightarrow e^+e^-$. Data (crosses) are compared to a NLO calculation (solid line, scaled) based on the NLO CTEQ6.1 PDFs.

data, however, the variance of the extracted d -valence density is now larger than before due to more freedom in the d_v parametrisation that is being used [8].

Another possibility to exploit the measurement of W bosons in $p\bar{p}$ collisions is provided by the fact that the u -quark momentum in the proton is larger than the d -quark momentum. As a result, W^+ -bosons in $p\bar{p}$ collisions are boosted along the direction of the incoming proton, while W^- -bosons will prefer the antiproton direction. The resulting W charge asymmetry can be used to constrain PDFs further and, because antiquark terms are enhanced at low E_T , has the potential of differentiating between sea and valence contributions.

1.2 Final states

As discussed in the previous paragraph the quark-gluon structure of the proton can be well described by NLO DGLAP evolution equations. The parton density functions extracted from data are however by far dominated by measurements of the inclusive DIS cross section. It is therefore an important cross check to confront predictions based on these PDFs to final state measurements.

The production of heavy flavours in ep scattering boasts multiple scales: the photon virtuality Q^2 , the heavy quark transverse momentum p_T and the heavy quark mass m_q . In NLO QCD, different approaches are used to calculate cross section for processes with heavy quarks in the final state. In the so-called Variable Flavour Scheme (VFS), one assumes that a heavy quark can be present in the initial state, giving the proton a heavy flavour content. This scheme resums terms proportional to $[\alpha_S \ln(Q^2, p_T^2/m_{c,b}^2)]^n$. In the Fixed Flavour Scheme (FFS), on the other hand, terms proportional to $[\alpha_S \ln(Q^2, p_T^2/m_{c,b}^2)]^n$ are neglected and heavy quarks are produced in the interaction itself. If calculations could be performed for all orders in perturbation theory, both schemes should yield the same result, as follows from the QCD factorisation theorem. Up to a fixed order in perturbation theory, however, differences occur and one has to choose a scheme that fits best with the kinematics of the process under study.

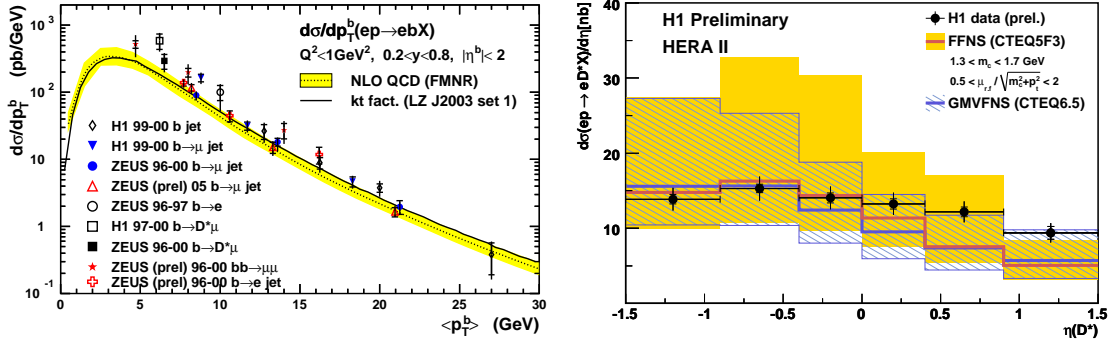


Fig. 4: (left) Differential cross section for $ep \rightarrow ebX$ as a function of p_T^b as obtained in various analyses. The result is compared to a Fixed Flavour Scheme calculation (FMNR). (right) Differential cross section for $ep \rightarrow eD^*X$ as a function of $\eta(D^*)$. The result is compared to a Fixed Flavour Scheme calculation (FFNS) and a Variable Flavour Scheme calculation (GMVFNS).

Figure 4 shows the transverse momentum and rapidity spectrum for bottom and charm quark, respectively, produced in photo-production interactions at HERA [13]. Overall, NLO QCD provides a good description of the data, although the mass and scale uncertainties are often larger than the experimental errors. At forward rapidity ($\eta > 0$) there is a hint that higher order predictions might be needed to provide a better description of the data.

In general, the NLO pQCD description of jet production in ep scattering works well [10]. However, when looking at specific jet final states, one can show that higher orders and/or different evolution dynamics are needed to describe all corners of phase space. Typically, this involves looking at small- x processes where multiple gluon radiation is enhanced. Figure 5 shows dijet and trijet differential cross sections compared to NLO and NNLO pQCD calculations [11]. For dijets, the NLO ($O(\alpha_S^2)$) prediction clearly falls beneath the data, while the NNLO ($O(\alpha_S^3)$) calculation describes the data well. For trijets the NLO ($O(\alpha_S^3)$) calculation seems to suffice. However, when one or two of these jets are produced at forward rapidity, the fixed order QCD calculation again fail. It has been shown that different

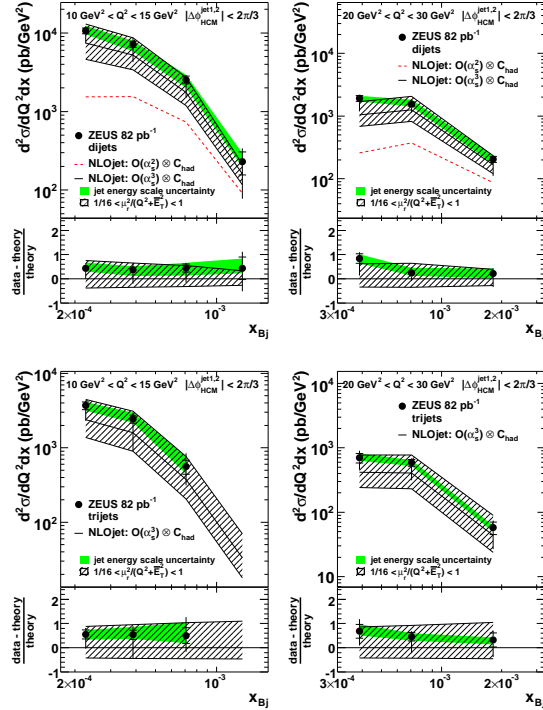


Fig. 5: The dijet and trijet cross section for events with $|\Delta\phi_{HCM}^{jet1,2}| < 2\pi/3$ as functions of x_{Bj} in two different Q^2 bins. The NLOJET calculations at $O(\alpha_S^2)$ ($O(\alpha_S^3)$) are shown as dashed (solid) lines.

at forward rapidity, the fixed order QCD calculation again fail. It has been shown that different

QCD dynamics (such as non k_T ordered parton showers) may accommodate the data well [12].

2 Interpolation region

A large part of the sessions on the interpolation region at the ISMD08 conference was dedicated to the study of diffractive interactions. In single diffractive dissociation (SDD), $pp \rightarrow pX$, one of the protons survives the interaction while the other dissociates in a hadronic system with invariant mass M_X , separated from the first proton by a large rapidity interval devoid of particles. In the presence of a hard scale, such interactions may be regarded as the result of the exchange of a colourless object with vacuum quantum numbers (e.g. a pomeron) consisting of quarks and gluons. One defines $\xi = 1 - \frac{P'}{P_L}$ as the fractional longitudinal momentum loss of the surviving proton and $t = (P - P')^2$, the squared four-momentum exchange at the proton vertex, with P and P' the four-momenta of the initial and scattered proton, respectively, measured in the initial state centre-of-mass frame.

In an optics analogon diffraction can also be called "shadow scattering" and is therefore inherently linked with the dense system upon which the incoming wave scatters. E.g. the t -slope of the diffractive cross section is related to the size of the dense system. Nevertheless to a large extend the description of diffractive interactions can be based on the same concepts as used for dilute systems and as such the study of diffractive interactions combines elements from both dense and dilute systems.

In this section, recent developments in diffractive scattering presented at ISMD08 are reviewed. The emphasis lies on the determination of the so-called "rapidity gap survival factor" and its implications on central exclusive production of various final states in pp scattering.

2.1 Measuring diffractive parton density functions

Diffractive deep-inelastic scattering (DDIS), $ep \rightarrow e\gamma^*p \rightarrow eXp$, occurs through the fusion of a virtual photon emitted by the electron and a colourless object exchanged by the proton (see Fig. 6a). Besides the usual deep-inelastic scattering variables, x and Q^2 , and diffractive variables, M_X , ξ (here called $x_{\mathbb{P}}$) and t , one defines $\beta = x/x_{\mathbb{P}}$ as the momentum fraction of the pomeron carried by the struck quark.

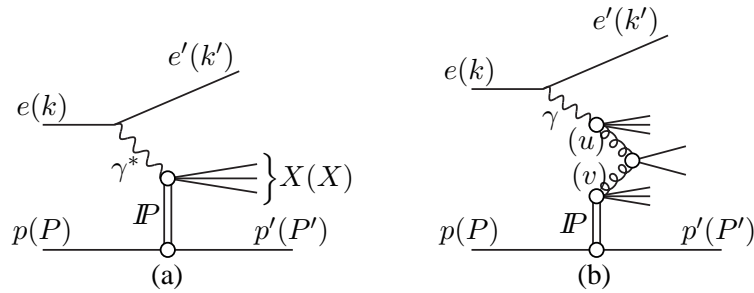


Fig. 6: (a) Diagram representing a diffractive deep-inelastic scattering interaction. (b) Diagram representing diffractive photoproduction. The four-momenta of the particles involved are given in parentheses

The HERA experiments use different methods for selecting diffractive interactions. In the rapidity gap method, one requires a large interval in rapidity devoid of particles. The kinematics of the event is then reconstructed from the dissociation system X . The four-momentum squared

t is not measured but integrated over. Another possibility is to extract a diffractive event sample from a fit to the M_X distribution. The non-diffractive background falls off exponentially towards low M_X and a fit of the form $D + C \exp(b \ln M_X^2)$ will yield the diffractive contribution D . As in the rapidity gap method, the kinematics of the event is measured from the X system and, again, one integrates over t . The most straightforward method is direct proton tagging with forward proton detectors. In this case, a pure single diffractive event sample is obtained without any contamination by proton dissociation events and a direct reconstruction of t is possible through the measurement of the proton four-momentum.

Figure 7 shows, as an example, the DDIS cross section obtained with the large rapidity gap method by the ZEUS and H1 experiments. Good agreement, within experimental uncertainties, is obtained between both experiments. A remaining normalisation difference of 13% is covered by the uncertainty on the proton dissociation correction (8%) and the relative normalisation uncertainty (7%). Results obtained with different selection methods also agree well.

In the QCD analysis of DDIS one assumes two different forms of factorisation. QCD hard scattering factorisation has been theoretically proven to hold in DDIS [15] and separates the partonic hard scattering cross section σ^{ei} , for the interaction between the electron and a quark i out of the proton, from a so-called diffractive parton density function (DPDF) f_i^D , which describes the probability to find a quark inside the proton under the condition that the proton survives the interaction with kinematics described by $x_{\mathbb{P}}$ and t :

$$\sigma^{ep \rightarrow eXY} = f_i^D(x, Q^2, x_{\mathbb{P}}, t) \cdot \sigma^{ei}(x, Q^2). \quad (2)$$

Proton vertex (or Regge) factorisation on the other hand is only approximately satisfied. Nevertheless, it is used successfully in the parametrisation of the DDIS cross section. This fac-

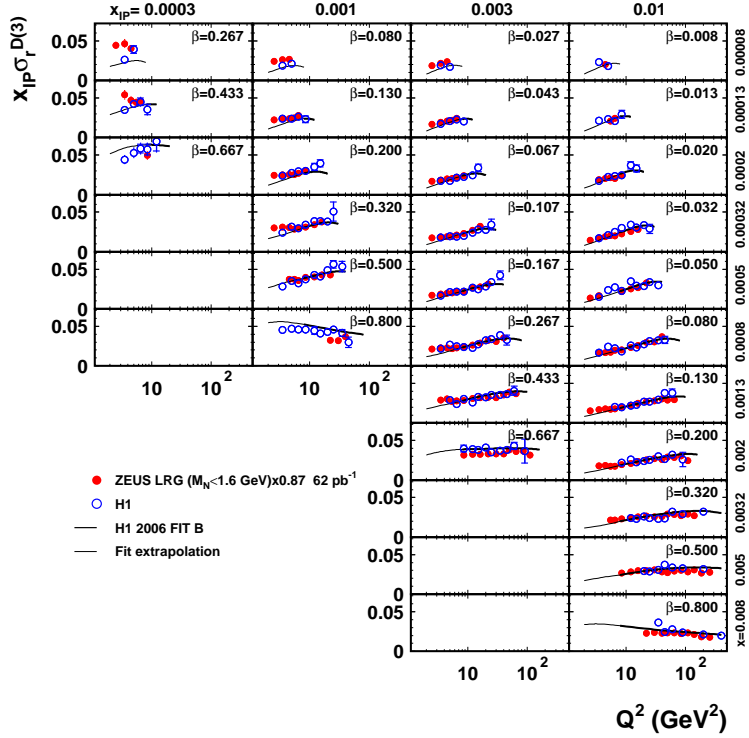


Fig. 7: The reduced cross section $\sigma_r^{D(3)} = \frac{d\sigma^D}{dx_{\mathbb{P}} dx dQ^2} / \frac{4\pi\alpha^2}{xQ^4} \left(1 - y + \frac{y^2}{2}\right)$ is plotted against Q^2 in bins of x and $x_{\mathbb{P}}$. H1 and ZEUS data are compared to the H1 2006 Fit B (see further in the text). A normalisation difference between ZEUS and H1 data is not shown (the ZEUS data points are scaled down by 13%).

torisation assumption expresses the DPDF as a superposition of pomeron and reggeon terms separating the flux factors $f_{\mathbb{P}/p}$ and $f_{\mathbb{R}/p}$ of pomerons and reggeons in the proton from their partonic structure $f_i^{\mathbb{P}}$ and $f_i^{\mathbb{R}}$:

$$f_i^D(x, Q^2, x_{\mathbb{P}}, t) = f_{\mathbb{P}/p}(x_{\mathbb{P}}, t) \cdot f_i^{\mathbb{P}}(\beta = \frac{x}{x_{\mathbb{P}}}, Q^2) + n_{\mathbb{R}} f_{\mathbb{R}/p}(x_{\mathbb{P}}, t) \cdot f_i^{\mathbb{R}}(\beta = \frac{x}{x_{\mathbb{P}}}, Q^2). \quad (3)$$

Here $n_{\mathbb{R}}$ is factor describing the relative normalisation of reggeon to pomeron fluxes. The fluxes themselves are obtained from a parameterisation inspired by Regge Theory where the $x_{\mathbb{P}}$ dependence is governed by the parameter $\alpha_{\mathbb{P}}(0)$.

A NLO QCD fit can be performed yielding values for $\alpha_{\mathbb{P}}(0)$, $n_{\mathbb{R}}$ and a polynomial for the quark and gluon densities at a fixed starting scale Q_0^2 . Usually, the reggeon flux is fixed and its parton density is taken to be equal to that of the pion.

The H1 collaboration obtained two fits (labelled *A* and *B*) using different polynomial forms for the gluon distribution at the starting scale (see Fig. 8) [16]. Both have similar good χ^2 values of 158/183 d.o.f. and 164/184 d.o.f., respectively. The quark distributions are found to be very stable in both fits, while the gluon distributions agree at low values of z but vary at high z .

One way of confirming the validity of the above approach and to differentiate between fit *A* and *B* is to take the parton distributions as obtained from a fit to the inclusive DDIS data and apply them to describe an exclusive channel such as DDIS dijet production. This channel is expected to be particularly sensitive to the gluon content of the pomeron, also at high z . Fit *A* is in good agreement with the DDIS dijet cross section at low $z_{\mathbb{P}}$, but overshoots the data at high $z_{\mathbb{P}}$. Fit *B*, however, is in good agreement with the data at all $z_{\mathbb{P}}$ [17]. This comparison therefore confirms QCD factorisation in DDIS and favours fit *B* obtained from inclusive data. Including the jet data in a combined fit of dijet and inclusive DDIS data yields a unique result with $\chi^2 = 196/218$ d.o.f., where both the quark and gluon distribution are constrained with similar good precision. The resulting parton densities lie close to Fit *B* and are the most precise to date.

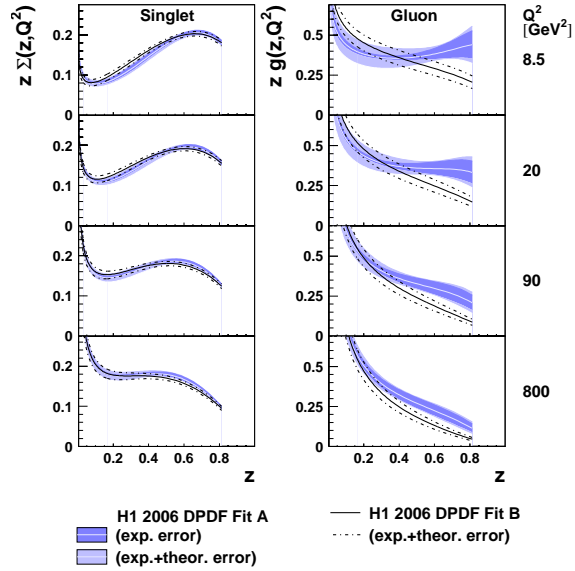


Fig. 8: The quark (singlet) and gluon densities as obtained in a NLO QCD fit are shown as function of fractional momentum z at different scales Q^2 . Two fits are obtained based on different parameterisations of the gluon density at the starting scale Q_0^2 .

2.2 Survival probabilities

Although the DPDFs extracted from a fit to inclusive DDIS data from HERA can be used to predict other DDIS channels such as dijet production, they fail to describe diffractive jet production

in proton-proton scattering at the TEVATRON by a factor of 10. This is to be expected, as QCD factorisation is not supposed to hold in proton-proton diffraction: multi-pomeron exchanges, remnant interactions or screening may lead to additional particle production, thereby destroying the rapidity gap. These effects can be parametrized as a rapidity gap survival probability and a lot of theoretical and experimental effort now goes to the determination of this factor.

One way to study the rapidity gap survival within one experiment is provided in electron-proton diffractive photoproduction (DPHP). In this process, $ep \rightarrow e\gamma p \rightarrow eXp$, a quasi-real photon emitted by the electron interacts diffractively with the proton (see Fig. 6b) to produce a central hadronic system X . If this system has a hard scale, one may define $x_\gamma = P \cdot u/P \cdot q$ as the fractional momentum from the photon entering the hard interaction and $z_P = q \cdot v/q \cdot (P - P')$ as the fractional momentum from the colourless exchange transferred to the hard interaction. The four-momenta used in the above formulae are defined in the figure.

One can compare interactions where the quasi-real photon interacts as a whole to interactions where the photon is resolved in a hadron-like structure so that only part of the photon's momentum enters the dijet system. Experimentally, both cases can be distinguished by reconstructing the variable x_γ : direct photon interactions will have a reconstructed value of x_γ close to 1, while resolved photon interactions will have lower values for x_γ . One should note however that the separation between direct and resolved photon interactions in theoretical calculations is only possible at fixed order, as additional orders will move part of the direct photon cross section at lower order to the resolved photon cross section.

Both the H1 and ZEUS collaborations have studied the rapidity gap survival probability by measuring the x_γ dependence of the cross section for diffractive dijet production [18]. Surprisingly, although both experiments do observe a suppression of the measured cross section when compared to the theoretical prediction without survival factor, neither experiment finds a strong dependence on x_γ (see Fig. 9). As a result, no evidence has been found for any difference in survival probability for interactions mediated by resolved and direct photons. A difference in the observed survival factor between H1 and ZEUS has been traced back to different cutoffs in jet E_T and a harder E_T slope in data compared to NLO theory.

The measurement of diffractive production of vector bosons in pp collisions provides another possibility to study rapidity gap survival. Moreover, this process is also sensitive to the quark component of DPDFs.

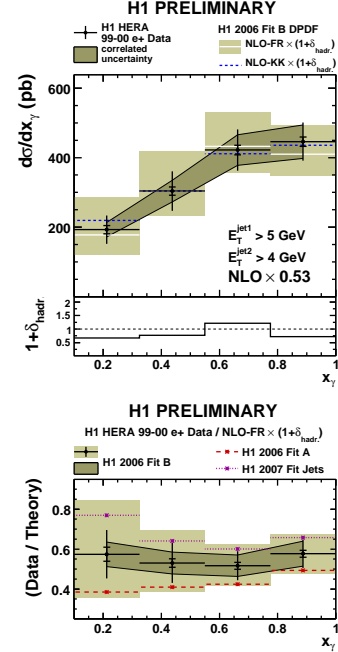


Fig. 9: Differential cross section and ratio of data over theory for diffractive photoproduction of dijets as function of x_γ measured by H1.

2.3 Central exclusive production at the TEVATRON

Double pomeron exchange (DPE), $pp \rightarrow pXp$, is the process where both protons survive the interaction, whilst a central hadronic system with invariant mass M_X is produced through the fusion of two colourless objects (often assumed to be pomerons). In hard central exclusive production (CEP), the central hadronic system boasts a hard scale (transverse momentum, invariant mass, . . .) with no soft remnants present in the final state X .

Central exclusive production in pp collisions is a particularly interesting channel for the discovery or study of the Higgs because this channel has some advantages over inclusive channels: QCD $b\bar{b}$ backgrounds are suppressed due to the $J_z = 0$ spin selection rule, an accurate determination of the Higgs mass is possible through the measurement of the outgoing proton momenta and azimuthal angular correlations may shed information on the spin-parity of the Higgs-candidate. Given the large uncertainty on the rapidity gap survival factor, a data-driven calibration is however mandatory. Here the observation of central exclusive production of dijets, diphoton, χ_c particles, etc. may serve to calibrate models. The calculation in [20] predicts a CEP standard model Higgs cross section of 3 fb at the LHC. In particular scenarios of MSSM and NMSSM, CEP may be the most probable channel for a discovery [24].

The CDF collaboration searched for CEP of dijets by looking for an excess in the distribution of the dijet mass fraction $R_{jj} = \frac{M_{jj}}{M_X}$ in DPE events [19]. Events where dijets are produced exclusively should show up at $R_{jj} \approx 1$. In Fig. 10 the observed R_{jj} distribution is compared to the POMWIG Monte Carlo model. This model uses DPDFs extracted from data as input but does not include exclusive production of dijets. An excess of data over the POMWIG prediction is observed at high R_{jj} , indicating that exclusive dijet events are present in the data. As a cross-check, a similar search was made for an excess of b -tagged jets. Such an excess was not found, as is expected due to spin selection rules.

After applying further selections to enhance the exclusive signal, a fit to the data distributions of R_{jj} was made using the sum of POMWIG and specific models for CEP of dijets with a free normalisation of the CEP models. Two models have been used: ExHuME, which is based on a LO pQCD calculation [20], and DPEMC, which is an exclusive DPE Monte Carlo model based on Regge Theory [21]. Both models are able to describe the excess at high R_{jj} well. However, when looking at the jet E_T distribution, the ExHuME model is favoured. This model also describes the M_{jj} distribution reasonably well.

Other CEP final states have also been investigated by the CDF Collaboration. In a sample

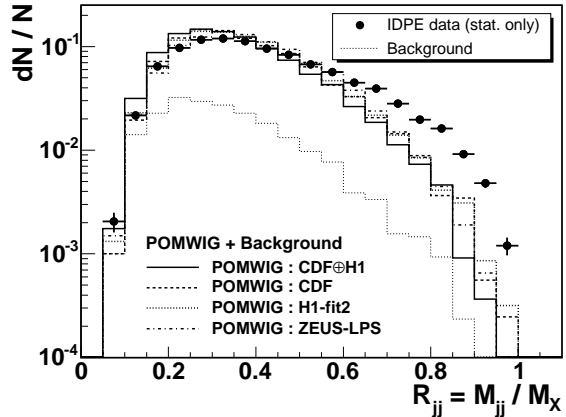


Fig. 10: (left) The R_{jj} distribution observed in DPE data (points) is compared to predictions by POMWIG (histograms) based on different DPDFs extracted from data.

of 532 pb^{-1} of Run-II data, 3 exclusive diphoton events were found with $E_T^\gamma > 5 \text{ GeV}$ and $|\eta^\gamma| < 1$ [22]. Exclusive production of dileptons can occur through two-photon exchange and is a nearly pure QED process. Using the same dataset as above, CDF found 16 candidate events with $E_T^e > 5 \text{ GeV}$ and $|\eta^e| < 2$, over an expected background of 1.9 ± 0.3 [23].

3 Dense systems

The approximations made for dilute systems will fail once the parton density becomes large enough. As observed at HERA, the proton structure function F_2 rises steeply towards small fractional momenta x . If continued unabided, this rise would violate unitarity conditions, even in the perturbative regime where $Q^2 \gg \Lambda^2$. One therefore expects new parton dynamics to show up at low x , resulting in a saturation of the growth of the parton density towards smaller x .

When parton densities become large, the linear approximation of Sec. 1 is no longer applicable. At high parton density, nonlinear fusion processes will start to balance parton branchings. Moreover, the collinear and k_T factorisation assumptions in perturbative QCD will become invalid, which means that higher twist contributions become important and that parton scatterings are no longer incoherent.

Saturation is expected to occur when partons are numerous enough and extended enough to overlap each other. This happens at low x and low Q^2 . A simple estimate of the saturation scale is therefore given by the ratio of the parton density to the area of the target. Assuming the gluon density in the nucleus to be given by $G_A(x, Q^2) = Ag(x, Q^2)$, with A the atomic mass number and $g(x, Q^2)$ the gluon density inside the proton, the saturation scale for nuclei would be given by

$$Q_s^2 \propto \alpha_S \frac{x G_A(x, Q_s^2)}{\pi R_A^2} \propto A^{1/3} x^{-\lambda}, \quad (4)$$

where the last equation makes use of the fact that the nuclear radius $R_A \propto A^{1/3}$ and that the gluon density in the proton rises exponentially towards small x with exponent $\lambda \approx 0.3$.

From Eq. 4 one can deduce that saturation effects are amplified in heavy nuclei by a factor $A^{1/3}$. At RHIC, with d -Au collisions at 200 GeV, the saturation scale is given by $Q_s^2 \approx 2 \text{ GeV}^2$. For p -Pb collisions at the LHC, with a centre-of-mass energy of 8.8 TeV, the saturation scale rises up to 5 GeV^2 .

3.1 Probing the matter created at RHIC

In a dense, strongly coupled medium, the propagation of high momentum, strongly interacting partons is expected to be impeded. This has been observed in heavy ion collisions at RHIC by looking at the nuclear modification factor $R_{AA}(p_T)$ which is defined as the ratio of particle yields in heavy ion collision to pp collisions, corrected for the number of collision partners [25]. As can be seen in Fig. 11 (left) a suppression is indeed observed for hadrons, but not for photons as should be the case because photons do not carry any colour charge. Moreover, the suppression for hadrons is not observed in periferal collisions where the medium is less dense. The same conclusion can be reached from Fig. 11 (right) where one looks for the away-side jet in proton and gold collisions [26]. While pp and p -Au data do show the presence of the away-side jet, it

disappears in central Au-Au collisions indicating the effect of the dense medium. At high p_T , however, the away-side jet reappears, showing that it is possible to “punch through” the dense medium, as long as the initial momentum is high enough.

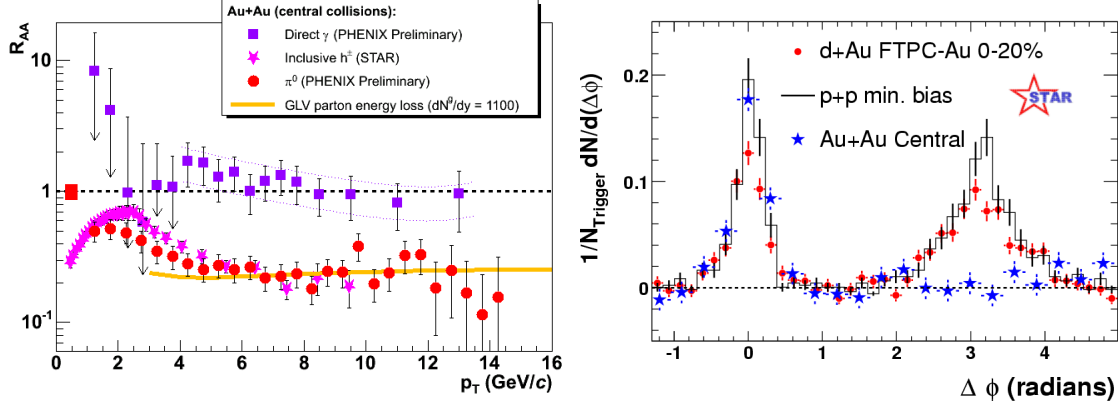


Fig. 11: (left) Nuclear modification factor as function of transverse momentum for direct photons, charged hadrons and neutral pions in central Au-Au collisions at 200 GeV centre-of-mass energy [27]. (right) Azimuthal correlation of charged hadrons with $p_T > 2$ GeV associated to a trigger particle with $4 \text{ GeV} < p_T < 6 \text{ GeV}$ [28].

For a quantitative understanding of these effects, one needs to constrain model parameters. Here the transport coefficient \hat{q} , defined as the average transverse momentum transferred per unit length, and gluon density dN_g/dy will play a major role. For this, more sophisticated observables are being used, such as di-hadron correlation function and fragmentation functions.

3.2 Saturation in heavy ion collisions from RHIC to LHC

The dense, strongly coupled nature of the medium probed in central heavy ion collisions at RHIC has thus been established. One has also found indications for the onset of saturation at RHIC. The charged hadron multiplicity at central rapidities is lower than predicted by all but a few models. Among those models giving a correct value are those which include saturation effects. The dependence of the charged hadron multiplicity on the centrality and centre-of-mass energy of the collision is consistent with geometrical scaling, which implies that the hadron multiplicity grows as the number of initially released gluons (assuming local parton-hadron duality) which is just proportional to the saturation scale [31]. Finally, Fig. 12 shows that, while d -Au collisions do not exhibit a suppression in R_{AA} for hadrons produced at central rapidities, a suppression does occur for hadrons produced at large rapidity [32]. This forward hadron suppression is well described by models based on saturation.

The rise of the saturation scale Q_s^2 from 2 GeV^2 for 200 GeV d -Au collisions at RHIC to 5 GeV^2 for 8.8 TeV p-Pb collisions at the LHC means that the LHC will be able to study saturation with perturbative probes. The ALICE Collaboration will study saturation effects with forward jets but also with low p_T open charm production at central rapidity.

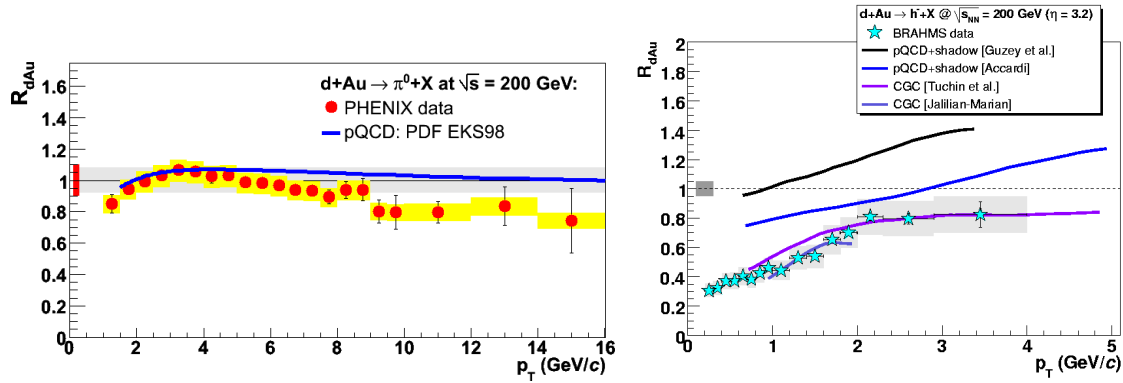


Fig. 12: Nuclear modification factors in deuterium-gold collisions for centrally (left) and forwardly (right) produced hadrons [29].

4 Strategies and analysis methods

In dense systems, the probability for additional activity besides the primary parton-parton interaction is large. One distinguishes two effects: the underlying event (UE) is caused by soft reinteractions between the remnants of the incoming particles, while multi-parton interactions (MPI) are due to multiple hard parton-parton interactions occurring in the same collision.

A good description of UE and MPI effects is crucial in the study of high energy hadron interactions. These effects may modify jet pedestals, mask missing energy or complicate isolation criteria. MPIs may even fake discovery signals, e.g. the MPI cross section for $pp \rightarrow W b\bar{b}X$, where the W boson and $b\bar{b}$ pair are produced in separate parton-parton interactions, may constitute an important background to Higgs production at the LHC via W -Bremsstrahlung, $pp \rightarrow WHX$, with the Higgs boson decaying to a $b\bar{b}$ pair. Several models for UE and MPI effects exist in the form of tunes of the PYTHIA Monte Carlo program to TEVATRON data. However, the extrapolation to higher energy yields wide uncertainties on the magnitude of these effects at the LHC. It will therefore be of crucial importance to tune UE and MPI models with early LHC data

In the following, I will review some of the techniques, presented at ISMD08, which are used to study the effect of UE and MPI. As will be seen, detectors placed near the beamline in order to detect forward scattered particles play an essential role in the study of various high density effects, including QCD evolution and saturation.

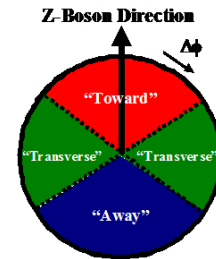


Fig. 13: Definition of “toward”, “away” and “transverse” region in azimuth w.r.t. the direction of the Z -boson created in $p\bar{p} \rightarrow ZZ$ interactions.

4.1 Observables for studying underlying events and multi-parton interactions

The underlying event will produce additional soft particles next to the hard scattering component. It can therefore be beneficial to divide the phase space into different regions with respect to the direction of the hard scattering products and to look at various event properties in these

regions. In Fig. 13 this principle is applied to Drell-Yan production of lepton pairs via the process $p\bar{p} \rightarrow ZX$. One may then define observables like the charged particle multiplicity, the scalar transverse momentum sum of charged particles or the average or maximum transverse momentum of charged particles in each region. Some examples are given in Fig. 14. A excellent agreement with PYTHIA tune “AW” is observed. The close match with leading jet UEs is perhaps indicating a universality of underlying event models irrespective of the hard scattering event [33].

Multi-parton interactions will induce long range correlations in particle production: whereas in single interaction events the central particle multiplicity does not depend strongly on forward activity, one does expect a strong correlation between central particle multiplicity and forward energy [35]. Figure 15 shows the dependence of central particle multiplicity on forward energy depositions for different MPI scenarios. Clearly, in the absence of MPI, very little correlation is observed. A measurement of this correlation at the LHC may help to differentiate between different MPI tunes based on TEVATRON data.

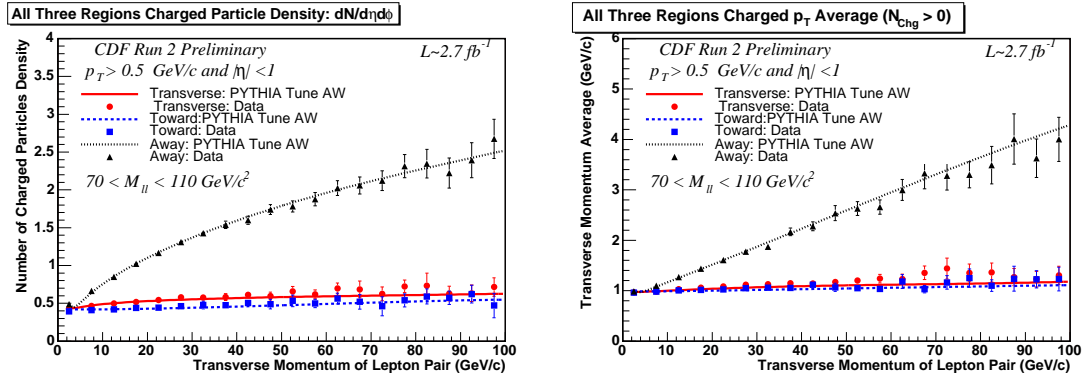


Fig. 14: Dependence of charged multiplicity (left) and average transverse momentum (right) on the p_T of the Z -boson created in $p\bar{p} \rightarrow ZX$ interactions in different region in azimuth. The effect of the recoil quark back-to-back to the Z -boson is clearly visible. Data are compared to the PYTHIA “AW” tune.

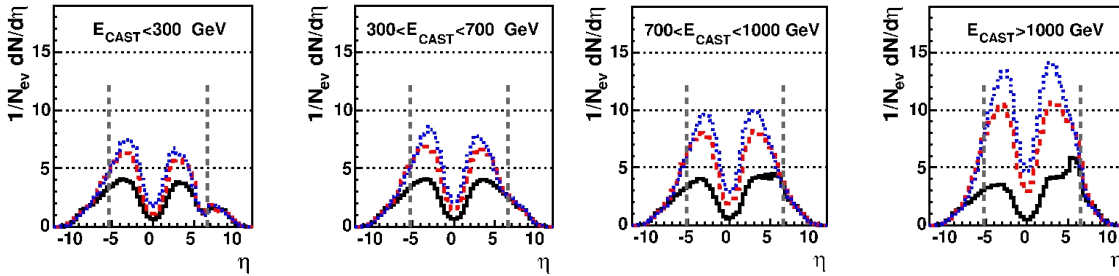


Fig. 15: Simulated rapidity distribution for particles in pp collisions produced at the LHC with different conditions on energy deposited in the forward region. E_{CAST} is defined as the energy sum of charged particles with $5.2 < \eta < 6.6$ and $p > 1$ GeV. The black histograms was obtained with MPI simulation turned off, while the coloured histograms represent different tunes for MPI implemented in PYTHIA.

4.2 Forward physics

Both the ATLAS and CMS Collaboration plan the installation of several detector near to the outgoing proton direction in order to detect forward scattered particles. The main detectors have calorimetric coverage up to values of pseudorapidity $|\eta| < 3$. Outside this range the ATLAS and CMS detector include forward calorimeters (FCAL and HF) covering the pseudorapidity range of $3 < |\eta| < 5$. Beyond this, the ATLAS Collaboration will install a luminosity detector (LUCID) covering $5.5 < |\eta| < 6.2$. In CMS, a similar pseudorapidity range, $5.2 < -\eta < 6.6$, will be covered by a calorimeter (CASTOR), albeit only on one side of the experiment. Both collaborations plan furthermore to install Zero Degree Calorimeters and Roman Pot detectors along the beam line. Also the TOTEM Collaboration, which shares the same interaction point as CMS, will install trackers and Roman Pot detectors close to the beam line. An overview of the coverage in pseudorapidity and transverse momentum is given in Fig. 16.

At low Bjorken- x , partons may undergo long parton showers before they meet to form the hard scattering subsystem. Forward particles can then be produced in two ways: (i) a collision between a low- x and a high- x parton will boost the hard scattering subsystem forward; (ii) a collision between two low- x partons will produce a central hard scattering system while forward jets may result from gluons radiated in the parton shower.

A large imbalance in Bjorken- x will result in a hard scattering subsystem X that is produced forward. X can be jets, Drell-Yan pairs, prompt photons, heavy quark pairs, etc. The relation between the Bjorken- x of the low- x parton and the pseudorapidity of the hard scattering system is given by $x = \frac{Q}{\sqrt{s}}e^{-\eta}$, which yields $x \geq 10^{-6}$ for $Q \geq 10 \text{ GeV}$ and $\eta = 6$ at the LHC. Figure 17 shows the kinematic plane of M vs. x for the production of forward Drell-Yan pairs with invariant mass M . CASTOR will be able to measure the energy deposits of Drell-Yan e^+e^- pairs with $M \lesssim 30 \text{ GeV}$ and $x < 10^{-5}$. In this kinematic region one expects large shadowing effects in the proton parton densities. One calculation using the PYTHIA Monte Carlo generator based on a *saturated* parton density function [36] yields a reduction by a factor 2 w.r.t. the prediction based on the CTEQ5L parametrisation [37].

When both partons involved in the hard scattering have similar, low x , a dijet system will be produced centrally in the detector. Forward jets may then result from parton showers. BFKL-like QCD evolution will result in a larger cross section for high energy forward jets, as can be seen in Figure 17. Also jet-gap-jet or Mueller-Navelet jet topologies are particularly sensitive to different approaches for QCD evolution.

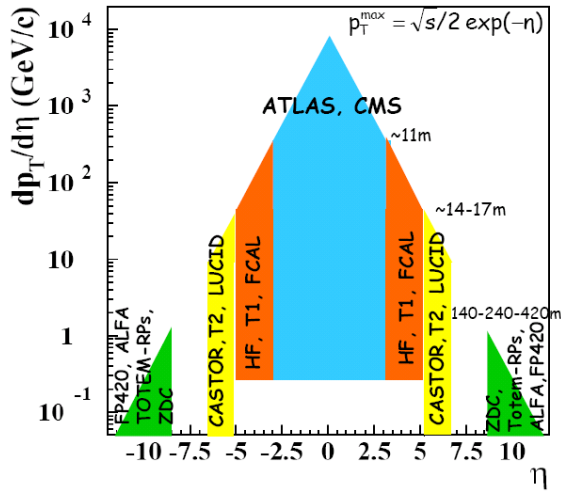


Fig. 16: Coverage in p_T and η of different subdetectors constructed and planned by the ATLAS, CMS and TOTEM Collaborations at the LHC.

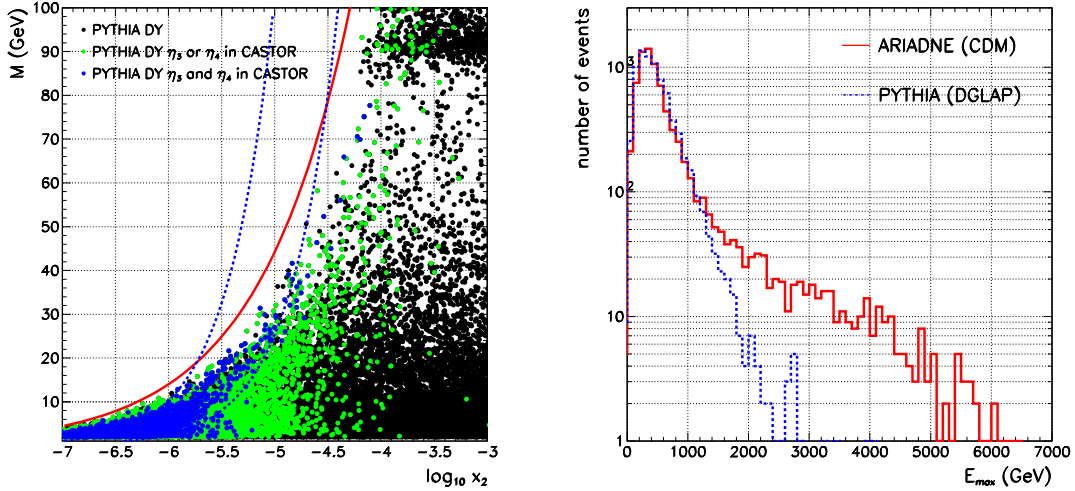


Fig. 17: (left) Kinematic plane of invariant mass M vs. x for Drell-Yan pairs at generator level. The full line gives the kinematic limit $M_{max} = \sqrt{x_2 s}$, while the dashed lines show the acceptance limits $M = x_2 \sqrt{s} \exp^y$, $y \in [5.2, 6.6]$ of the CASTOR calorimeter. Green (blue) dots indicate Drell-Yan pairs where at least one (both) electron(s) are within the CASTOR acceptance. (right) Distribution of generator-level jet energy in CASTOR for events with hard central dijets ($p_T > 60$ GeV and $|\eta| < 3$) as obtained from a PYTHIA simulation using the standard DGLAP evolution [38] (dashed line) and the colour dipole model implemented in ARIADNE [39] (full line).

5 New physics

Many different scenarios exist for physics beyond the Standard Model, ranging from compositeness over supersymmetry to the existence of extra dimensions. It is clearly impossible to review all final states that are being scrutinized by running and future experiments in this experimental summary. For this, I refer to the relevant contributions to these proceedings. Here, I will focus on model independent searches for new physics and the status of Standard Model Higgs searches at the TEVATRON and the LHC.

5.1 Global search for physics beyond the Standard Model

Data collected in Run II of the TEVATRON have been searched for indications of new electroweak scale physics. Rather than focusing on particular new physics scenarios, CDF data have been analyzed for discrepancies with the Standard Model prediction. A model-independent approach (Vista) considers gross features of the data, and is sensitive to new large cross section physics. A quasi-model-independent approach (Sleuth) emphasizes the high- p_T tails, and is particularly sensitive to new electroweak scale physics. An algorithm has been developed to search invariant mass distributions for “bumps” that could indicate resonant production of new particles. As can be seen in Fig. 18, this combined global search for new physics in 2.0 fb^{-1} of $p\bar{p}$ collisions at $\sqrt{s} = 1.96$ TeV reveals no indication of physics beyond the Standard Model [40].

The H1 collaboration too has performed a model-independent search for deviations from

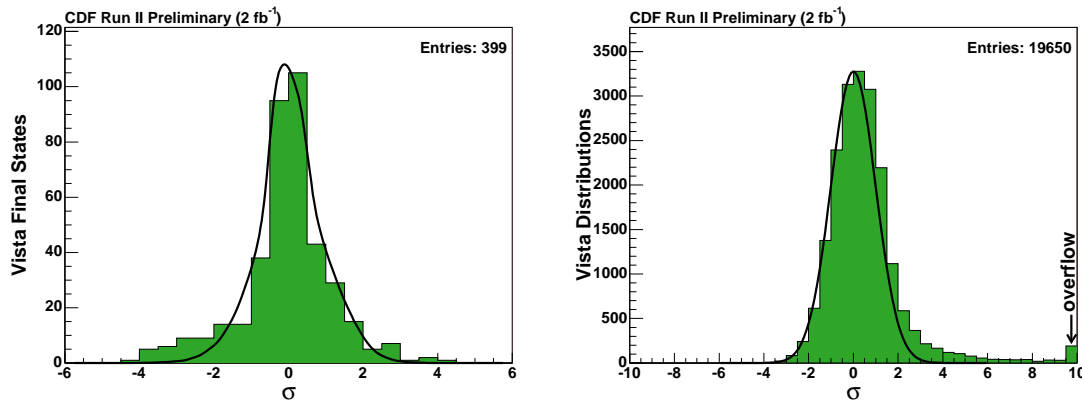


Fig. 18: (left) Graphical summary of Vista final state population discrepancies showing the number of standard deviations from the Standard Model prediction. No final state shows a significant population discrepancy, after accounting for the trials factor. (right) Graphical summary of Vista kinematic variable distribution discrepancies. Interest is focused on the outliers, representing distributions with significant discrepancy. However, after analysis, none of these discrepant distributions motivate a new physics claim.

the Standard Model. Both e^+p and e^-p collisions from the HERA II run are used, corresponding to 178 pb^{-1} and 159 pb^{-1} , respectively. All event topologies involving isolated electrons, photons, muons, neutrinos and jets with high transverse momenta are investigated in a single analysis. Events are assigned to exclusive classes according to their final state. A statistical algorithm is used to search for deviations from the Standard Model in the distributions of the scalar sum of transverse momenta or invariant mass of final state particles and to quantify their significance. A good agreement with the Standard Model prediction is observed in most of the event classes. Figure 19 shows that no significant deviation is observed in the phase-space and in the event topologies covered by this analysis [41].

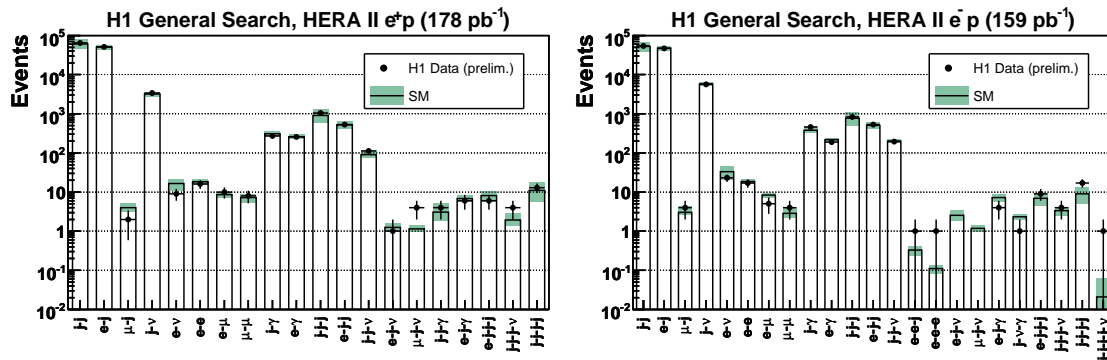


Fig. 19: The data and SM expectation for all event classes with observed data events or SM expectation greater than 1 event: (left) e^+p data, (right) e^-p data.

If new physics beyond the SM is around, the LHC experiments will see it in most of the

cases. The observation and identification of supersymmetric reaction channels will require as many measurements as possible, including cross sections, branching ratios, masses and spins. Various methods will be used and are thoroughly being prepared [42].

5.2 Standard Model Higgs searches at the TEVATRON and LHC

The CDF and D0 collaborations have each combined their search results in single full mass range exclusion plots. The 95% CL exclusion limits lie around 4 and 2 times the Standard Model cross sections for $m_H = 115$ GeV and $m_H = 170$ GeV, respectively (see Fig. 20 (left-top)). A TEVATRON wide combination of low mass exclusion limits is challenging because of the large number of channels involved. An exclusion limit of around 3 times the Standard Model cross section at $m_H = 115$ GeV is however expected if CDF and D0 results would be combined. At high mass, a Standard Model Higgs particle with $m_H = 170$ GeV is now excluded at 95% CL by the combined CDF and D0 data, as is shown in Fig. 20 (left-bottom). A larger exclusion zone around 170 GeV will probably follow soon.

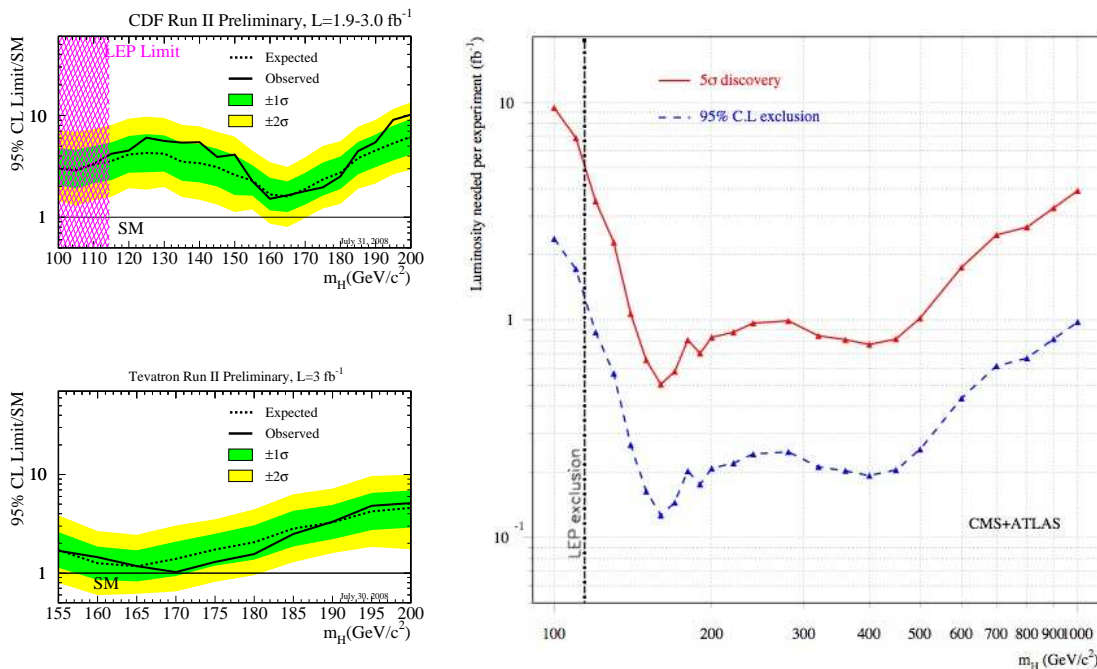


Fig. 20: (left-top) Observed and expected (median, for the background-only hypothesis) 95% CL upper limits on the ratios to the SM cross section, as functions of the Higgs boson mass between 100 and 200 GeV/c² for the combined CDF data. The bands indicate the 68% and 95% probability regions where the limits can fluctuate, in the absence of signal. (left-bottom) Observed and expected 95% CL upper limits at high masses as obtained from the combined CDF and D0 data. (right) The prospects for discovering a Standard Model Higgs boson in initial LHC running, as a function of its mass, combining the capabilities of ATLAS and CMS.

A light Standard Model Higgs particle therefore seems most likely. This happens to be the

most challenging region, also at the LHC. Figure 20 (right) shows the luminosity needed for a discovery or 95% CL exclusion at the LHC. 5 or 1 fb^{-1} are needed for a 5σ discovery or 95% CL exclusion, respectively [44].

Acknowledgments

I would like to thank the organisers of ISMD08 for their hospitality and the invitation to DESY, Hamburg. I acknowledge the hard work of all speakers and gladly refer to individual contributions in these proceedings for more detailed information on the topics presented during the symposium.

References

- [1] V. N. Gribov, L. N. Lipatov, Sov. J. Nucl. Phys. 15 (1972) 438; *ibid.* 15 (1972) 675; L. N. Lipatov, Sov. J. Nucl. Phys. 20 (1975) 94; G. Altarelli and G. Parisi, Nucl. Phys. B126 (1977) 298; Yu. L. Dokshitzer, Sov. Phys. JETP 46 (1977) 641.
- [2] E. A. Kuraev, L. N. Lipatov and V. S. Fadin, Sov. Phys. JETP 44 (1976) 443; *ibid.* 45 (1977) 199; I. I. Balitsky and L. N. Lipatov, Sov. J. Nucl. Phys. 28 (1978) 822.
- [3] M. Ciafaloni, Nucl. Phys. B296 (1998) 49; S. Catani, F. Fiorani and G. Marchesini, Phys. Lett. B234 (1998) 339; *ibid.* Nucl. Phys. B336 (1990) 18; G. Marchesini, Nucl. Phys. B445 (1995) 49.
- [4] A. M. Cooper-Sarkar, *Extraction of the proton parton density functions using a NLO-QCD fit of the combined H1 and ZEUS inclusive DIS cross sections*, Proc. of XVI Int. Workshop on Deep Inelastic Scattering and Related Topics, London, England, April 2008, <http://dx.doi.org/10.3360/dis.2008.25>.
- [5] V. Chekelian, *Neutral Current DIS with polarized e^+ / e^- at HERA*, Proc. of the XXXIII Int. Conference on High Energy Physics, Moscow, Russia, July-August 2006.
- [6] V. Chekelian, *A measurement of the longitudinal proton structure function $F_L(x, Q^2)$ at high Q^2 at HERA*, Proc. of the XVI Int. Workshop on Deep Inelastic Scattering and Related Topics, London, England, April 2008, <http://dx.doi.org/10.3360/dis.2008.39>.
- [7] D0 Collaboration, Phys. Rev. Lett. 101 (2008) 062001.
- [8] G. Watt, A. D. Martin, W. J. Stirling, R. S. Thorne, *Recent Progress in Global PDF Analysis*, Proc. of the XVI Int. Workshop on Deep Inelastic Scattering and Related Topics, London, England, April 2008, <http://dx.doi.org/10.3360/dis.2008.22>.
- [9] S. Malik, *PDF constraints from CDF*, Proc. of the XVI Int. Workshop on Deep Inelastic Scattering and Related Topics, London, England, April 2008, <http://dx.doi.org/10.3360/dis.2008.26>.
- [10] M. Gouzevitch, *Jet cross sections and α_S in DIS*, Proc. of the XVI Int. Workshop on Deep Inelastic Scattering and Related Topics, London, England, April 2008, <http://dx.doi.org/10.3360/dis.2008.171>.
- [11] ZEUS Collaboration, Nucl. Phys. B786 (2007) 152-180.
- [12] H1 Collaboration, Eur. Phys. J. C46 (2006) 27-42.
- [13] A. W. Jung, *D^* meson production in DIS and photoproduction with the H1 detector at HERA*, Proc. of the XVI Int. Workshop on Deep Inelastic Scattering and Related Topics, London, England, April 2008, <http://dx.doi.org/10.3360/dis.2008.196>. U. Samson, *Beauty photoproduction at ZEUS*, Proc. of the XVI Int. Workshop on Deep Inelastic Scattering and Related Topics, London, England, April 2008, <http://dx.doi.org/10.3360/dis.2008.189>.
- [14] M. Ruspa, *Inclusive Diffraction in DIS with the ZEUS detector*, Proc. of the XVI Int. Workshop on Deep Inelastic Scattering and Related Topics, London, England, April 2008, <http://dx.doi.org/10.3360/dis.2008.65>.
- [15] J. Collins, Phys. Rev. D57 (1998) 3051 [Erratum-*ibid.* D61 (2000) 019902]
- [16] H1 Coll., Eur. Phys. J. C48 (2006) 715-748.

- [17] H1 Coll., JHEP 0710:042, 2007.
- [18] K. Černý, *Diffractional photoproduction of dijets in ep collisions at HERA*, Proc. of the XVI Int. Workshop on Deep Inelastic Scattering and Related Topics, London, England, April 2008, <http://dx.doi.org/10.3360/dis.2008.69>; ZEUS Coll., Eur. Phys. J. C55 (2008) 177-191.
- [19] CDF Coll., T. Aaltonen et al., Phys. Rev. D77, 052004 (2008).
- [20] J. Monk and A. Pilkington, Comput. Phys. Commun. 175, 232 (2006); V. A. Khoze, A. D. Martin and M. G. Ryskin, Eur. Phys. J. C14, 525 (2000).
- [21] M. Boonekamp and T. Kucs, Comput. Phys. Commun. 167, 217 (2005); A. Bialas and P. V. Landshoff, Phys. Lett. B256, 540 (1991).
- [22] CDF Coll., T. Aaltonen et al., Phys. Rev. Lett. 99, 242002 (2007).
- [23] CDF Coll., A. Abulencia et al., Phys. Rev. Lett. 98, 112001 (2007).
- [24] M. Tasevsky, S. Heinemeyer and V. Khoze *Central exclusive diffractive MSSM Higgs boson production by forward proton tagging at the LHC* and J. Forshaw, *NMSSM Higgs Boson Production with Tagged Protons*, Proc. of the XVI Int. Workshop on Deep Inelastic Scattering and Related Topics, London, England, April 2008, <http://dx.doi.org/10.3360/dis.2008.84> and <http://dx.doi.org/10.3360/dis.2008.86>.
- [25] STAR Coll., Phys. Rev. Lett. 91 (2003) 072304
- [26] STAR Coll., Phys. Rev. Lett. 90 (2003) 082302; *ibid.* 97 (2006) 162301.
- [27] D. G. d'Enterria, Eur. Phys. J. C 43 (2005) 295 [arXiv:nucl-ex/0504001].
- [28] C. Adler *et al.* [STAR Collaboration], Phys. Rev. Lett. 90 (2003) 082302 [arXiv:nucl-ex/0210033].
- [29] D. G. d'Enterria, J. Phys. G 34 (2007) S53 [arXiv:nucl-ex/0611012].
- [30] H. Caines, these proceedings.
- [31] N. Armesto, C. A. Salgado, U. A. Wiedemann, Phys. Rev. Lett. 94 (2005) 022002.
- [32] A. Dainese, these proceedings.
- [33] D. Kar and R. Field, CDF/PUB/CDF/PUBLIC/9351, July 24, 2008.
- [34] CDF Coll., Phys. Rev. Lett. 79, 584 (1997)
- [35] Z. Rurikova, *Underlying event studies with Castor calorimeter in CMS experiment*, at "HERA and the LHC A workshop on the implications of HERA for LHC physics", CERN, May 2008.
- [36] A. Dainese et al., *Small-x effects in heavy quark production*, Proc. of the HERA and the LHC workshop, March 2004 - March 2005; K. J. Eskola et al., Nucl. Phys. B660 (2003) 211.
- [37] H. L. Lai et al., Eur. Phys. J. C12 (2000) 375 - 392.
- [38] T. Sjöstrand, S. Mrenna and P. Skands, JHEP 05 (2006) 026.
- [39] L. Lönnblad, Comput. Phys. Commun. 71 (1992) 15.
- [40] C. Henderson, *Results of a model-independent global search for new physics at CDF*, Proc. of the XLIIIth Rencontres de Moriond: QCD and High-Energy Interactions, La Thuile, Italy, March 2008, arXiv:0805.0742v1 [hep-ex].
- [41] E. Sauvan, *A general search for new phenomena at HERA*, Proc. of 15th Int. Workshop on Deep-Inelastic Scattering and Related Subjects, Munich, April 2007, <http://dx.doi.org/10.3360/dis.2007.73>.
- [42] W. Ehrenfeld, *Supersymmetry and other beyond the Standard Model physics: Prospects for determining mass, spin and CP properties*, these proceedings, ATL-PHYS-PROC-2008-075.
- [43] CDF and D0 Collaborations, *Combined CDF and D0 upper limits on Standard Model Higgs boson production at high mass (155–200 GeV²/c²) with 3 fb⁻¹ of data*, Proc. of the XXXIV International Conference on High Energy Physics, ICHEP08, July 29-August 5, Philadelphia, USA, arXiv:0808.0534v1 [hep-ex].
- [44] J.-J. Blaising et al., *Potential LHC contributions to Europe's future strategy at the high-energy frontier*, CERN Council Strategy Group, Briefing Book Volume 2, <http://council-strategygroup.web.cern.ch>.